# Temperature-induced stochastic resonance in Kerr photonic cavities for frequency shift

**Bertrand Braeckeveldt**[1,*] **and Bjorn Maes**[1]

[1] *Micro- and Nanophotonic Materials Group, Research Institute for Materials Science and Engineering, University of Mons, 20 Place du Parc, Mons B-7000, Belgium*

[*] *bertrand.braeckeveldt@umons.ac.be*

**Abstract:** Driven non-linear photonic cavities are widely studied because they exhibit many interesting effects, such as non-reciprocity, thermal effects and frequency conversion. Specifically, adding noise to a modulated non-linear system can lead to stochastic resonance (SR), which corresponds to periodic transitions between stable states. In this work, we study the outgoing power and spectra from a non-linear driven photonic cavity coupled to an external port. Using a Langevin framework, we show that the system temperature induces SR in the bistable regime, which we study in detail to exploit for enhanced frequency shift. In this way, the thermal fluctuations of the system itself can function as a driver for effective sideband generation, enabling shift efficiencies of up to 40%. We extensively explore various regimes in order to understand and maximize the process.



## 1. Introduction

Dynamic modulation of photonic structures is an important subject nowadays, with exotic effects and important applications. For example, it can be used for reciprocity-breaking to achieve optical isolation without using magnetic materials [1–4]. Temporal modulation can also be used for selective frequency conversion, when applied in coupled cavities [5]. Recently, for thermal emission, an active cooling mechanism was reported, with thermodynamic performance approaching the Carnot limit [6]. On a fundamental level, driven non-linear systems can exhibit numerous interesting dynamical phenomena [7]. Specifically, when driven out of equilibrium, the resonances can be used for amplification of fluctuations [8], generation of squeezed states [9] or stochastic resonance (SR) [10].

When considering a non-linear, periodically modulated bistable system, the appearance of SR is well known [10–12]. With SR the addition of a particular amount of noise in the system leads to an amplification of its response. A fundamental model is the particle in a double well potential. The particle cannot escape from its current state, associated to one of the wells, if the potential is modulated through an external (weak) periodic force. However, by adding random thermal fluctuations of energy $k_B T$, Kramers shows [13] that the particle can now escape in a characteristic time $\tau_K$, decreasing exponentially with the ratio $\Delta U / k_B T$, with $\Delta U$ the potential barrier. SR arises when the modulation period is twice the escape time $\tau_K$, resulting in the typical two transitions per period at the correct noise level [10].

SR is now applied in many fields, going from physics [14–25], finance [26–28], chemistry [29–32], biology [33–40] to social [41, 42] science. Most of the studies, and the current work, assume the Markov approximation. However, recent works deal with memory effects e.g. in non-linear optical systems, where it has been employed for energy harvesting enhancement [43].

In this work, non-linearity (of the Kerr type), temporal modulation and thermal noise are combined. We exploit the noise from thermal fluctuations inherent in the system due to a non-zero temperature. Temporal modulation is a clear pathway towards novel frequency-conversion devices, and here we introduce enhanced shift via temperature-induced SR in a bistable photonic cavity. Evidently, the process is governed by a host of different parameters, and we identify and examine the important ones in detail. In this way we can provide insight into maximizing the shift of a pump wave into a particular sideband frequency.

Beside the frequency shift, which is the coherent component of the cavity output, we also examine the incoherent part, which is the thermal emission. This extends the study on thermally activated transitions, leading to strongly enhanced thermal fluctuations, which were examined in a photonic framework of a bistable driven system [44].

The paper is structured as follows. In Sec. 2, we present the numerical model and detail the system parameters. Sec. 3 contains the results with subsections for the important parameters. We first demonstrate (Sec. 3.1) that temperature-induced noise can lead to SR, and elucidate the temperature roles. Then we vary the modulation frequency (Sec. 3.2). Next, the detuning and signal amplitude are studied (Sec. 3.3 and 3.4), with consequences on outgoing power and frequency shift. Finally, we discuss the losses and the coupling factor between cavity and waveguide (Sec. 3.5 and 3.6). In a separate section (Sec. 4) we explore thermal radiation with temporal modulation, with the notable supernarrow peaks, as expected [45].

## 2. Numerical model

We consider a single Kerr non-linear photonic cavity coupled to an external port, which could be implemented as schematically shown in Fig. 1(a). Various equivalent designs with e.g. a photonic crystal cavity are also possible [46–51]. The cavity is driven by a pump via the channel, and coupled to internal and external baths at temperatures $T_d$ and $T_e$, respectively. In such a general system, the cavity mode amplitude evolution is efficiently described using coupled-mode theory and the Langevin framework [44, 52]:

$$\frac{\mathrm{d}a}{\mathrm{d}t} = \left[j\left(\omega_0 - \alpha|a|^2\right) - \gamma\right] a + \sqrt{2\gamma_e}s_+ + \sqrt{2\gamma_d}\xi_d, \tag{1a}$$

$$s_+ = s_p e^{j\omega_p t} + \xi_e, \tag{1b}$$

$$s_- = -s_+ + \sqrt{2\gamma_e}a \tag{1c}$$

with $|a|^2$ normalized, representing the cavity mode energy, and $\omega_0$ the cavity resonance frequency. Incoming and outgoing power from/into the external channel are given by $|s_+|^2$ and $|s_-|^2$, respectively. The incoming wave $s_+$ consists of both a pump (with frequency $\omega_p$ and amplitude $s_p$) and thermal radiation $\xi_e$, arising from the external bath at temperature $T_e$. We will add modulation to the pump later on. The coupling between cavity and port is controlled via the decay rate $\gamma_e$. While $\gamma_d$ represents the internal dissipation of the cavity, for example arising from coupling to phonons (absorption), which leads to a coupling with an internal bath at temperature $T_d$ via $\xi_d$. The sum of these quantities defines the total dissipation rate $\gamma = \gamma_e + \gamma_d$. The Kerr non-linearity is described by the coefficient $\alpha$, which is chosen to be positive and real (leading to self-phase modulation, and no two-photon absorption) [44, 52]. Therefore, the system will provide dispersive bistability, as opposed to absorptive bistability [16]. Assuming a narrow bandwidth ($\gamma \ll \omega_0$), the noise sources $\xi_i (i \in \{e, d\})$ are delta-correlated with an intensity given by the mean energy of Planck's oscillator $\Theta(\omega_0, T_i) = \hbar\omega_0/(\exp(\hbar\omega_0/k_B T_i) - 1)$. As in previous works [44, 52], we use the approximation of the classical limit for the noise intensity, $k_B T_i$.

Using a frame rotating at the pump frequency with $\delta\omega = \omega_0 - \omega_p$, $\tau = \delta\omega\ t$, $u =$

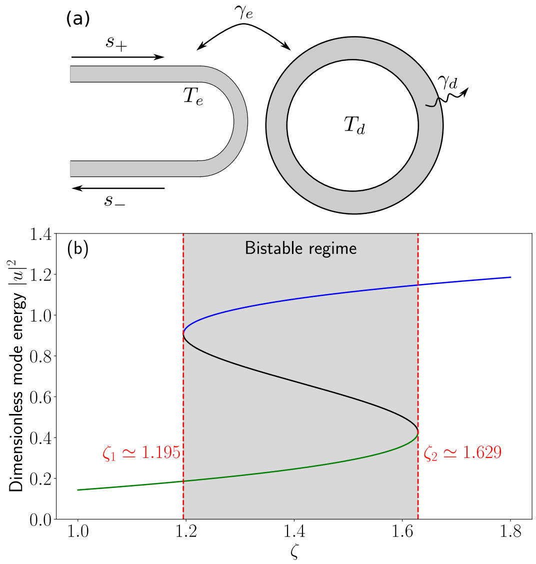


Fig. 1. (a) Simulated system composed of one non-linear photonic cavity coupled to an external channel at temperatures $T_d$ and $T_e$ respectively. (b) Hysteresis plot of the dimensionless mode energy versus non-linear coupling $\zeta = |\tilde{s}_p|^2$ and detuning $\Delta = -2.5$. Colors represent solutions described in Appendix B, $y_1$ in green, $y_2$ in black and $y_3$ in blue.

$\sqrt{\alpha/\delta\omega}a \exp(-j\omega_p t)$, one transforms Eq. (1a) to (1c) into

$$\frac{\mathrm{d}u}{\mathrm{d}\tau} = \left[j\left(1 - |u|^2\right) - \eta\right] u + \sqrt{2\eta^3}\tilde{s}_p + \sqrt{2n_d}\tilde{\xi}_d + \sqrt{2n_e}\tilde{\xi}_e, \tag{2a}$$

$$\tilde{s}_+ = \tilde{s}_p + \sqrt{\frac{n_e}{\eta^3}}\tilde{\xi}_e, \tag{2b}$$

$$\tilde{s}_- = -\tilde{s}_+ + \frac{\gamma_e}{\gamma}\sqrt{\frac{2}{\eta}}u, \tag{2c}$$

where $\eta = \gamma/\delta\omega$, $\tilde{\xi}_i = \xi_i/\sqrt{k_B T_i \delta\omega} \exp(-j\omega_p t)$, $n_i = \frac{\gamma_i \alpha k_B T_i}{\delta\omega^2}$ $(i \in \{e, d\})$, and $\tilde{s}_i = \sqrt{\frac{\alpha\gamma_e}{\gamma^3}} s_i \exp(-j\omega_p t)$ $(i \in \{+, -, p\})$. In Eq. (2a), $\tilde{\xi}_e$ and $\tilde{\xi}_d$ are uncorrelated noise sources satisfying [45]

$$\langle \tilde{\xi}_i^*(\tau)\tilde{\xi}_i(\tau')\rangle = \delta(\tau - \tau'), \tag{3a}$$

$$\langle \tilde{\xi}_i(\tau)\tilde{\xi}_i(\tau')\rangle = 0, \tag{3b}$$

$$\langle \tilde{\xi}_i^*(\tau)\tilde{\xi}_i^*(\tau')\rangle = 0, \tag{3c}$$

where $i \in \{e, d\}$ and $\langle . \rangle$ means taking the "thermodynamic ensemble average". These conditions can be realized by taking the real and imaginary parts of $\tilde{\xi}_i$ as independent random variables.

Defining the dimensionless detuning $\Delta = -\delta\omega/\gamma = (\omega_p - \omega_0)/\gamma$ and the effective non-linear coupling $\zeta = |\tilde{s}_p|^2$, one can show that the system is bistable if for the pump $\zeta_1 < \zeta < \zeta_2$ ($\zeta_1$ and $\zeta_2$ are functions of the detuning as described in Appendix A) and for the detuning $\Delta < -\sqrt{3}$ (example in Fig. 1(b)).

Now, we extend this model by applying temporal modulation through the pump with the addition of a signal at frequency $\omega_p + \Omega$, having a small amplitude compared to the initial pump. The pump is thus described by

$$\tilde{s}_p(\tau) = \sqrt{\zeta_0}\left(1 + \delta e^{j\tilde{\Omega}\tau}\right) \tag{4}$$

where $\delta$ and $\zeta_0$ are defined by

$$\delta = \kappa\left[\frac{\zeta_2+\zeta_1}{\zeta_2-\zeta_1} - \sqrt{\left(\frac{\zeta_2+\zeta_1}{\zeta_2-\zeta_1}\right)^2 - 1}\right], \tag{5a}$$

$$\zeta_0 = \frac{\zeta_2+\zeta_1}{2(1+\delta^2)}, \tag{5b}$$

with $\kappa \in [0, 1[$. Eq. (5a) ensures the system always stays in the bistable regime (shaded region of Fig. 1(b)) during the whole modulation cycle, whereas Eq. (5b) determines that the time-averaged (dimensionless) pump power $|\tilde{s}_p|^2$ is centered between $\zeta_1$ and $\zeta_2$ (so we are operating in the middle of the hysteresis curve of Fig. 1(b)). We use these conditions so that any jump between the bistable states is initiated by thermal fluctuations, and not via the pump, so we obtain a clear (subthreshold) SR.

In the end, the input wave consists of a strong pump, driving at frequency $\omega_p$, which is now weakly modulated with frequency $\Omega$. As a result, the signal varies the non-linear Kerr effect according to Eq. (2a), leading to a time modulated system.

Eq. (2a) belongs to the category of stochastic differential equations, so it cannot be solved using classical numerical solvers [53–56]. Thus, we use a homemade solver in *python* based on the Runge-Kutta method, which we have validated by recovering results of previous studies [44, 52].

## 3. Coherent results

In this section, we extensively explore how SR can be exploited for frequency shift towards the signal frequency ($\omega_p + \Omega$). We look at the role of the various parameters, and typically examine two figures of merit: the ratio between outgoing and incoming power at signal frequency $|s_-(\omega_p + \Omega)|^2/|s_+(\omega_p + \Omega)|^2$, and the shift efficiency from incoming pump to outgoing signal, defined as $|s_-(\omega_p + \Omega)|^2/|s_+(\omega_p)|^2$ (so outgoing power at the signal frequency compared to the incoming power at the pump frequency).

As the system contains many parameters, we analyse the effects of each parameter separately, while keeping the others constant as much as possible. Unless otherwise stated, the parameters are set so that the detuning $\Delta = -2.5$, the signal detuning $\Delta_s = \Omega/\gamma = 0.01$, the cavity life-time $Q = \omega_0/\gamma = 10^4$, the relative signal amplitude $\delta = 0.077$ ($\zeta_0 = 1.40$) and the ratio of dissipation rates $\gamma_e/\gamma_d = 1$.

### 3.1. Temperatures

First, we examine the onset of SR as a function of temperature, via Eq. (2a) to (5b). We first consider both baths with the same temperature ($T_e = T_d = T$). Increasing the temperature increases the probability to observe transitions between stable states. In Fig. 2(a)-(d), black dashed lines represent mode energies corresponding to potential extrema (see Appendix B). As the system is in the bistable regime, there are two minima and one local maximum for the potential. The upper branch corresponds to the stable state with the highest energy while the bottom one represents the lowest energy state. Finally, the central dashed line is related to the mode energy at the potential local maximum. The noisy red line represents a time traces of the dimensionless mode energy. Each figure coincides to a given temperature. The associated coherent output powers are presented in Fig. 2(e).

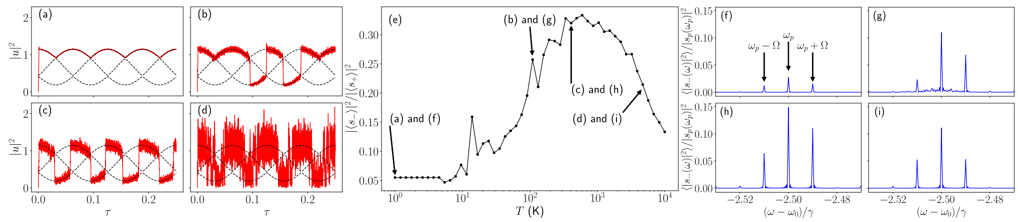


Fig. 2. (a)-(d) Time traces (red lines) of the dimensionless mode energy $|u|^2$ for different temperatures, with potential energy extrema indicated (black dashed lines). (a) $T = 1$ K, (b) $T = 100$ K, (c) $T = 400$ K, (d) $T = 5000$ K. (e) Coherent output power as a function of temperatures. SR arises for $T \simeq 400$ K (time trace (c)). (f)-(i) Spectral density of total outgoing power into the external channel, normalized by incoming power at pump frequency, for temperatures corresponding to time traces (a) to (d), respectively.

For low temperatures, Fig. 2(a), the system remains in the same modulated state corresponding to one of the potential minima represented by a dashed black line. As temperature increases, the system sometimes jumps to another branch (Fig. 2(b)). In this situation, the mode energy $|u|^2$, illustrated by the red line, sometimes hops from one minimum to another. At SR, Fig. 2(c), the cavity mode energy jumps with a frequency twice the modulation frequency, resulting in a synchronization between the modulation and the transitions [10]. In this situation, the output power (see Fig. 2(e)) is maximal as the system is more often in the lowest energy state. Indeed, somewhat counter-intuitively, the high energy state corresponds to large absorption, leading to small output power. For higher temperatures, Fig. 2(d), the transitions become very probable as thermal energy is high, causing very easy and more random crossings of the potential barrier.

The jump probability density function (PDF) is shown in Fig. 3(a) for temperatures of Fig. 2(b)-(d), so where there are transitions. As explained previously, there is a natural tendency for jumps to happen at odd multiples of the half modulation period ($T_\Omega/2$). Before SR ($T = 100$ K), the PDF decreases exponentially with time, but transitions peak at these odd multiples ($T_\Omega/2$, $3T_\Omega/2\ldots$). However, at SR ($T = 400$ K), the jumps occur periodically, leading to a narrow and centred PDF around half the modulation period (green graph). After SR ($T = 5000$ K), multiple transitions can be observed during one modulation period, because of the high noise intensity, leading to a broadened PDF (blue graph).

The coherent output power $|\langle s_- \rangle|^2$ as a function of temperature (Fig. 2(e)) is computed as follows. The coherent outgoing power at the three main frequencies (see Fig. 2(f)-(i)) are summed and compared to the summed input at the same frequencies ($\omega_p$ and $\omega_p \pm \Omega$). This ratio undergoes fluctuations for a small range of temperatures before SR (around $T = 10$ K), which correspond to a supernarrow peak in thermal radiation, as explained later in Sec. 4.

The spectral density of total output power is represented for various temperatures in Fig. 2(f)-(i), normalized by the incoming power at pump frequency $|s_p(\omega_p)|^2$. These temperatures are the same as for time traces of Fig. 2(a)-(d) and jump PDF of Fig. 3(a). At 1 K (Fig. 2(f)) the spectral density displays three main peaks. The central one, coincides with the pump frequency, $\omega_p$ as some incoming power is reflected. The two other peaks are separated by the modulation ($\Omega$) from the pump frequency. Indeed, even if there are no transitions (Fig. 2(a)) for such small temperatures (the PDF is therefore not shown in Fig. 3(a)), the steady state remains modulated. For 100 K (Fig. 2(b)) the peak amplitudes increase for the three frequencies. The amplitudes are maximised at SR (Fig. 2(h)), where the outgoing power is the highest (Fig. 2(e)). Beyond SR (Fig. 2(i)) the outgoing power at the three frequencies drops.

To better understand the role of the external ($T_e$) and internal ($T_d$) temperatures, we put one temperature to zero and vary the other one (Fig. 3(b)). The black curve is the same as in Fig 2(e)

($T_d = T_e = T$), whereas for the red curve, the internal bath is set to zero, $T_d = 0$ K ($T_e \neq 0$ K). The green curve denotes the opposite, with no external temperature, $T_e = 0$ K ($T_d \neq 0$ K). When both temperatures are equal, SR arises around 400 K (black dashed vertical line in Fig. 3(b)). However, with only one thermal source (red or green curve), we need around 800 K for SR (red dashed vertical line in Fig. 3(b)). Both temperatures are thus on equal footing here, and it is their sum that matters.

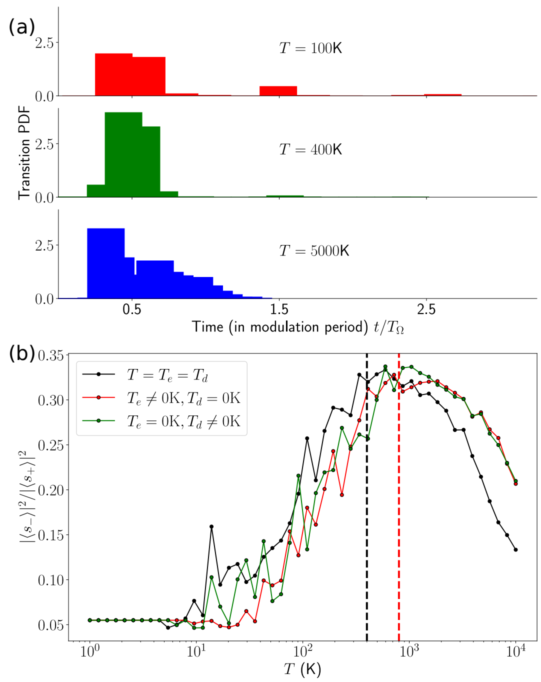


Fig. 3. (a) Jump probability density function between states for various temperatures. (b) Coherent output power as a function of temperature. The vertical dashed black line denotes SR when both temperatures are equal. The vertical dashed red line corresponds to SR when one temperature is set to 0 K.

### 3.2. Modulation frequency

Here, we vary the modulation frequency $\Delta_s = \frac{\Omega}{\gamma}$, while we keep $\gamma$ constant. We consider equal temperatures, so SR appears around 400 K with modulation frequency $\Delta_s = 0.01$ (as in Fig. 2). As shown in Fig. 4, with smaller modulation frequencies, SR happens at lower temperatures. As $\Delta_s$ decreases, the modulation of the state is slower. As a result, the system has more time to jump (via fluctuations) when the potential barrier is close to its minimum, and vice versa. Another way to understand this trend is remembering that SR corresponds to a synchronicity between the modulation frequency and the frequency of transitions between stable states. Transitions can therefore be less frequent for smaller modulation frequencies. As transition are induced by thermal energy, a lower temperature means a decrease of the transition frequency.

The frequency shift efficiency (right axis, Fig. 4) follows the same trend as the ratio between the outgoing and incoming power at signal frequency (left axis, Fig. 4). This shift efficiency is always the highest around SR, reaching 10% for the lower modulation frequencies. However, it drops to values close to 1% for the higher modulation frequencies. Therefore, increasing the modulation frequency ($\Delta_s$ in Fig. 4) deteriorates the shift efficiency and increases the temperatures to reach SR (with the maximum efficiency).

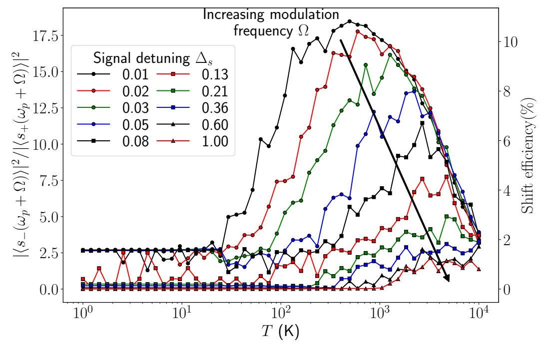


Fig. 4. Relative output power at signal frequency (left axis) and frequency shift efficiency (right axis) versus temperature for various modulation frequencies $\Delta_s = \frac{\Omega}{\gamma}$.

To summarise, the frequency shift efficiency is higher for slower modulations. Furthermore, SR, where this efficiency is the largest, appears at lower temperatures. However, as modulation corresponds to the signal, taking a smaller frequency, means a shift to a closer frequency. Therefore, there is a trade-off according to the desired goals (higher efficiency versus shift to larger frequency).

### 3.3. Detuning

Another important parameter is the (relative) detuning ($\Delta = \frac{\omega_p - \omega_0}{\gamma}$) between the pump and the cavity frequency. Note that a higher detuning $|\Delta|$ means that the pump frequency $\omega_p$ decreases with respect to the cavity resonance $\omega_0$ (the latter remaining constant). We keep $\Delta < -\sqrt{3}$, so the system is in the bistable regime (and SR is possible). Furthermore, as the limiting hysteresis pump powers ($\zeta_1$ and $\zeta_2$) are functions of the detuning (Appendix C), a change in the detuning modifies signal frequency power (Eq. (5a)). As we consider the effects of the relative input signal amplitude in the next section, $\delta$ is set to a constant value ($\delta = 0.0077$). Note that this is smaller than previously (where $\delta = 0.077$), but it is used here to reach detuning values close to the limit $-\sqrt{3}$ without exiting the bistable regime.

The parametric situation is shown in Fig. 5(a). This section sweeps along the horizontal red dashed line (detuning $\Delta$), while the next section sweeps along the vertical blue dashed line (signal amplitude $\delta$). In Fig. 5(a) the shaded region represents the bistable region, with pump and signal remaining below the jump thresholds, so the black dashed line represents the limit value for $\delta$. One can see that the acceptable signal amplitude decreases as we near the detuning $\Delta \simeq -\sqrt{3}$.

As detuning $|\Delta|$ increases, the frequency shift efficiency drops drastically, by several orders of magnitude (see Fig. 5(b)). The ratio between outgoing and incoming signal power (at $\omega_p + \Omega$) follows the same trend: from larger than $10^2$ to about 1 for the largest detuning ($\Delta = -5$). The required temperature to reach SR drastically increases as well when the detuning increases, so this parameter is crucial to control.

We note, for temperatures just below SR, there is a dip in the relative output power for all values of $\Delta$. This sudden drop is related to the drastic change in the thermal radiation spectra at these temperatures. Before stochastic resonance, the system presents a supernarrow peak in its thermal radiation spectrum as described in Sec. 4.

### 3.4. Signal amplitude

To explore the signal amplitude, we modify $\kappa$ (and thus $\delta$) in Eq. (5a). In contrast to the previous section, here the detuning is constant ($\Delta = -2.5$), but the signal amplitude is modified, see the blue dashed sweep line in Fig. 5(a). Furthermore, unlike the previous sections, the ratio between

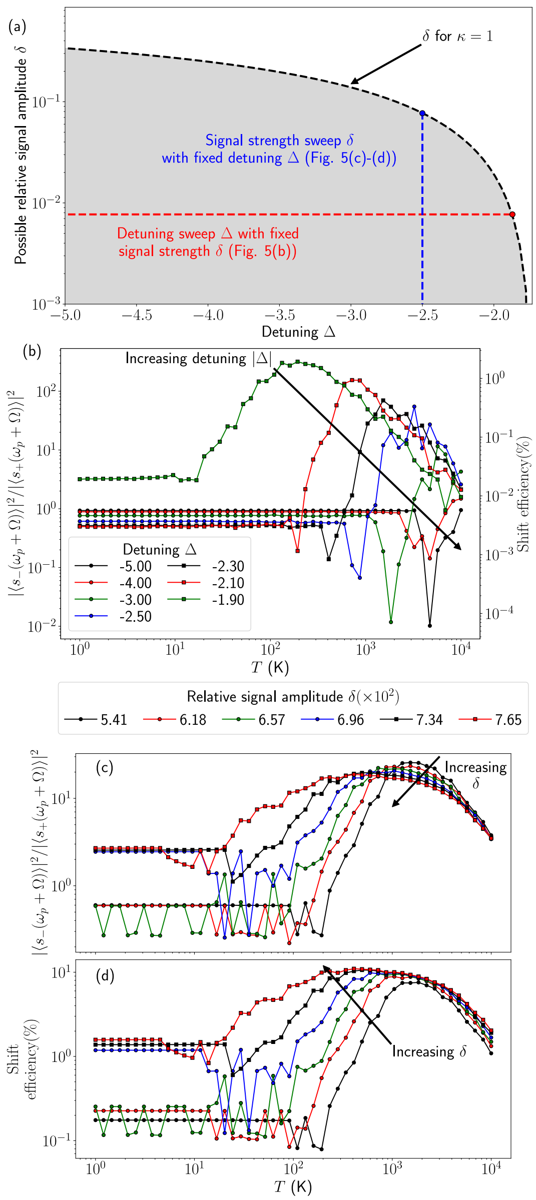


Fig. 5. (a) Illustration of the path followed during parameter sweeps of (b), (c) and (d) in a $(\delta, \Delta)$ space. (b) Relative output power at the signal frequency and shift efficiency for various detuning. (c) Relative output power at the signal frequency and (d) shift efficiency for various relative modulation amplitudes.

outgoing and incoming signal (Fig. 5(c)) and the shift efficiency (outgoing signal divided by incoming pump, Fig. 5(d)) do not follow the same trend. Indeed, the relation between both ratios is

$$\frac{|\langle s_-(\omega_p+\Omega)\rangle|^2}{|\langle s_+(\omega_p)\rangle|^2} = \underbrace{\frac{|\langle s_+(\omega_p+\Omega)\rangle|^2}{|\langle s_+(\omega_p)\rangle|^2}}_{\text{proportionality factor } p} \cdot \frac{|\langle s_-(\omega_p+\Omega)\rangle|^2}{|\langle s_+(\omega_p+\Omega)\rangle|^2} \tag{6}$$

so the proportionality factor $p$ depends on the coherent input powers. Previously, $p$ was constant, as the incoming power was always the same, so both quantities were plotted on the same graph (left and right axis, respectively). Here, however, we change the amplitude, so $p$ varies, and we need to represent the graphs separately.

When the signal amplitude $\delta$ increases, the outgoing power at signal frequency increases. However, the boost of outgoing power is smaller than the rise of incoming one. Therefore, the maximum (at SR) of the ratio between outgoing and incoming power at signal frequency (Fig. 5(c)) decreases for increasing $\delta$.

On the other hand, there is a gain in shift efficiency at SR for increasing signal amplitude $\delta$ (Fig. 5(d)), with SR reached for a smaller temperature as well. This last result can be expected. Indeed, for larger signal (increasing $\delta$), the potential barrier to cross at half modulation frequency decreases (see Appendix B). This is the reason why SR appears at larger temperatures for $\Delta = -2.5$ (blue curve in Fig. 5(b)) than in previous situation for the same detuning., Because the signal is ten times weaker in Fig. 5(b) ($\delta = 0.0077$) than in Fig. 2 ($\delta = 0.077$).

### *3.5. Total losses*

We now focus on the total losses $\gamma = \gamma_e + \gamma_d$, expressed via the cavity quality factor $Q = \omega_0/\gamma$, with equal rates for external and internal losses ($\gamma_e = \gamma_d$). Unequal external and internal ratios are discussed in the next section.

One must be careful with the parameter dependencies. For example, the detuning $\Delta$ is inversely proportional to $\gamma$, so we need to modify the pump frequency $\omega_p$, in order to keep $\Delta$ constant at $-2.5$. Furthermore, to keep a constant pump power, the ratio $\gamma^2/\alpha$ must also be constant as $s_p = \sqrt{\frac{\gamma^3}{\alpha\gamma_e}}\tilde{s}_p$. $\tilde{s}_p$ is already set because $\Delta$ is constant and $\frac{\gamma^3}{\alpha\gamma_e} = \frac{2\gamma^2}{\alpha}$, because the loss rates are equal. In the end, to keep the detuning and the input power constant, one also adjusts $\omega_p$ and $\alpha$.

From Fig. 6, decreasing the total loss (increasing $Q$) means the system reaches SR at higher temperature. Counter-intuitively, the frequency shift efficiency is larger when there are more losses (lower $Q$), so interestingly, more loss is more effective. However, this must be set against the fact that the non-linearity ($\alpha$) is also greater in this case.

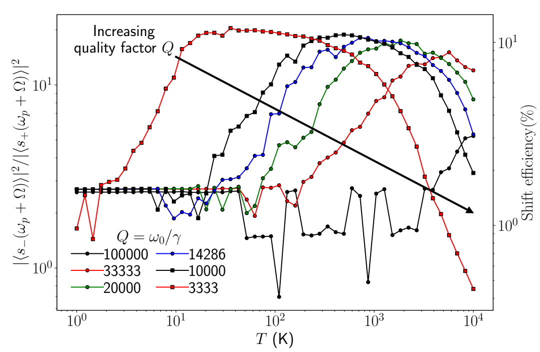


Fig. 6. Relative signal output power (left axis) and shift efficiency (right axis) versus temperature for various quality factors $Q = \omega_0/\gamma$.

### 3.6. Coupling

The coupling between the external channel and the cavity is controlled via $\gamma_e$. A large coupling means that the cavity energy is quickly lost via the external channel, and vice versa. Here, the ratio between external and internal losses $\gamma_e/\gamma_d$ is varied, while the total loss rate $\gamma = \gamma_e + \gamma_d$ is constant (so detuning $\Delta = -2.5$ and quality factor $Q = 10^4$ are also constant). Up to now, $\gamma_e/\gamma_d = 1$, so the system was at critical coupling, see the red (color online) vertical dashed lines in Fig. 7.

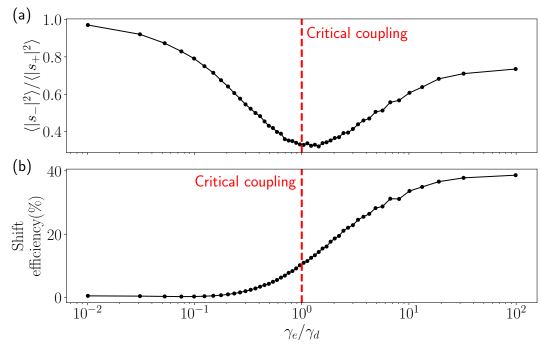


Fig. 7. (a) Output over input power ratio and (b) frequency shift efficiency at SR ($T = 400$ K) for varying ratios between external and internal losses.

By examining the ratio between the total output power and the total input power (Fig. 7(a)), we see that at critical coupling this ratio is minimal and smaller than 0.5. Thus, in this situation, most of the input power goes into the resonator and is absorbed. Furthermore, around this critical coupling point, the shift efficiency is around 10% when the system is in the SR regime (Fig. 7(b)), as already noted in previous sections.

In order to increase this efficiency, one can increase the external coupling or lower the internal losses. When the external losses are much larger than the internal ones, the shift efficiency is close to 40%, four times better than at critical coupling: so 40% of the input power at the pump frequency is shifted to output power at the signal frequency (thus shifted by $\Omega$). In this case, the output to input total power ratio is close to 0.7.

Conversely, when internal losses dominate, the shift efficiency is close to zero. This can be expected, as the power just reflects into the port, without interacting much with the resonator. Therefore, the output power is similar to the input power, and the reflection tends towards 1.

## 4. Thermal radiation

The thermal emission has interesting features, which we highlight in this section. In the system described by Eq. (2a) to (2c), the output thermal radiation can be computed as the difference between the total and coherent output, so for the spectral density of fluctuations for the thermal radiation this leads to $\langle|\delta s_-|^2\rangle = \langle|s_-|^2\rangle - |\langle s_-\rangle|^2$. As thermal radiation is, for the most part, incoherent, we are not interested specifically in its value at pump or signal frequencies.

When studying the spectral density of fluctuations of a bistable system, it is known that the system can undergo a kinetic phase transition (KPT) [45,57,58]. It arises when the transition rates between both states are equal, and occurs for a very narrow range of parameters. Furthermore, increasing the noise intensity beyond the KPT leads to SR [10,59]. The KPT is characterised by a supernarrow peak in the spectral density of fluctuations, so for thermal radiation in our case. For the parameters of Fig. 2, SR starts around 400 K, so we expect to see the supernarrow peak for lower temperatures, and it is already indicated by the noisy region around 10 K (as it is more difficult to distinguish thermal radiation from coherent output).

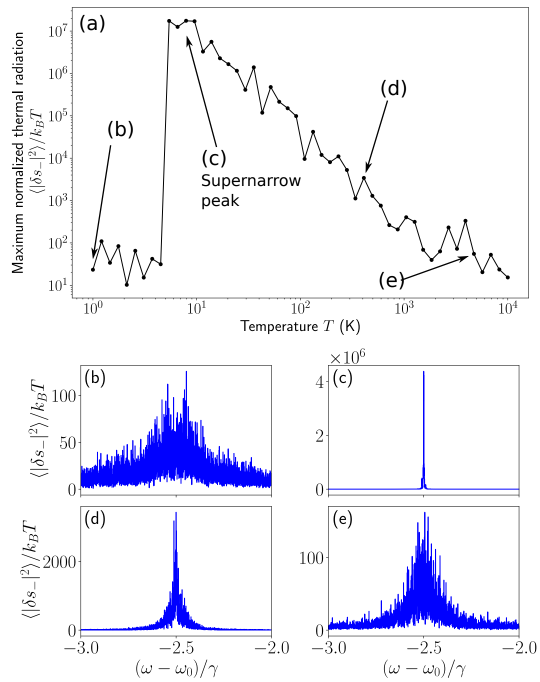


Fig. 8. (a) Normalized maximum thermal spectral density versus temperature. Normalized thermal spectral density at (b) $T$ = 1 K, (c) $T$ = 10 K, (d) $T$ = 410 K, (e) $T$ = 4715 K. For $T \simeq 10$ K, the thermal spectral density displays a supernarrow peak.

We observe these phenomena in the spectra at various temperatures (Fig. 8(b)-(e)). At 10 K (Fig. 8(c)), the thermal radiation is orders of magnitude larger than for lower and larger temperatures, and tightly centered around the pump frequency, which is characteristic of the supernarrow peak, and appears at lower temperatures than for SR as expected [59]. Analogously, the maximum thermal radiation for various temperatures (Fig. 8(a)) increases drastically around 5 K, associated with the supernarrow peak and the KPT. Beyond KPT, the maximum (normalized) thermal radiation decreases, with no particular effect for SR (Fig. 8(d)).

We note that the system parameters have similar effects on thermal radiation than on the coherent output power (discussed in the previous section): For example, the KPT arises for the same external or internal temperature, when one of them equals zero, the important parameter being the sum of both temperatures. (We remark that in the non-bistable regime, both temperatures do not have the same role, as interference between the external bath and the cavity mode can lead to Raman-type Stokes and anti-Stokes side peaks [44].) Furthermore, increasing the modulation frequency $\Omega$ shifts the supernarrow peak to higher temperatures and the peak amplitude decreases. Enlarging the detuning between the pump and the cavity has a similar consequence on the thermal radiation, leading to KPT at higher temperatures and a lower peak. Boosting the signal amplitude increases the maximum thermal radiation and KPT appears at lower temperatures. Finally, increasing losses in the system leads to a net rise of thermal radiation and shifts the supernarrow peak to lower temperatures as well.

## 5. Conclusion

We explored a resonant non-linear, driven cavity coupled to a waveguide. By injecting a signal at a frequency close to the pump frequency, in the bistable regime, the system undergoes a dynamic modulation via the Kerr non-linearity. The waveguide and cavity temperatures can then be controlled to thermally induce jumps between the states. The control of the frequency of these transitions, via the temperature of the system, can be used for frequency shift.

We demonstrate that the sum of both temperatures controls the appearance of SR, where hopping and modulation are synchronised, so that the outgoing power and the shift efficiency are maximised. The SR temperature and shift efficiency strongly depend on the system properties.

Faster modulation decreases the shift efficiency, but leads to a shift into higher frequencies. Moreover, larger temperatures are needed to optimise the shift and reach SR. Furthermore, increasing the detuning between pump and cavity frequency has similar effects, as a larger detuning leads to lower efficiencies at larger temperatures.

The shift efficiency increases for a larger signal, even if the ratio of outgoing over incoming signal power decreases. A larger signal reduces the SR temperature, however, for larger signals the system will already jump without fluctuations.

Enlarging the dissipation rates, while staying in the matched, critically coupled condition, improves the shift efficiency, however, this requires an increase of the non-linearity. We demonstrate that shift can be optimised by increasing the coupling between the cavity and the external port. With an external coupling rate much larger than the internal dissipation, we observe an efficiency close to 40%.

Finally, before reaching SR, the system undergoes a kinetic phase transition, where the thermal radiation presents a supernarrow peak. In this regime, thermal radiation is centered around the pump frequency and thus becomes monochromatic, with the peak orders of magnitude enlarged.

In order to obtain a frequency shift with resonance in the near-infrared domain, the silicon on silica structure presented by Khandekar et al. [52] can be used as a starting point. Indeed, their parameters are close to the one presented in our work. Furthermore, relatively fast electrical time-modulation can be applied to such structures [2]. As another highly promising technology for time-domain modulation, epsilon-near-zero materials, such as various transparent conducting oxides, offer a very strong non-linearity and extremely rapid time varying effects [60–64], which are both important to realise a temperature-induced frequency shift. In the end, our results prepare the way for enhanced, potentially integrated, frequency shift devices, stimulated purely by thermal processes.

## A. Steady-state solution

Thermal noise is neglected in first approximation due to its small contribution under the assumption $|s_p|^2 \gg \gamma k_B T$. Due to the pump, the steady-state dimensionless cavity energy $y = |u|^2$, is given by the cubic-equation [45, 65]

$$\frac{y}{\eta}\left[1 + \left(\frac{y-1}{\eta}\right)^2\right] = 2|\tilde{s}_p|^2. \tag{7}$$

The system is bistable if Eq. (7) admits only real solutions. Solutions of Eq. (7) are real if the polynomial

$$\mathcal{P}(y) = y^3 - 2y^2 + (1+\eta^2)y - 2\eta^3|\tilde{s}_p|^2 \tag{8}$$

satisfies $\mathcal{P}(y_+) < 0$ and $\mathcal{P}(y_-) > 0$ where $y_+$ and $y_-$ are the local minimum and maximum of $\mathcal{P}$ respectively, given by

$$y_\pm = \frac{2 \pm \sqrt{1-3\eta^2}}{3}. \tag{9}$$

These extrema are real if $\Delta < -\sqrt{3}$ and the two conditions lead to

$$|\tilde{s}_p|^2 > \frac{y_+^3 - 2y_+^2 + (1+\eta^2)y_+}{2\eta^3} = \zeta_1, \tag{10a}$$

$$|\tilde{s}_p|^2 < \frac{y_-^3 - 2y_-^2 + (1+\eta^2)y_-}{2\eta^3} = \zeta_2. \tag{10b}$$

In these equations, $|\tilde{s}_p|^2$ is a function of time given by Eq. (4) and these two relations must be satisfied for all times to remain in between the jump thresholds.

### B. Potential energy

The dimensionless system potential energy $U$ satisfies [66]

$$\frac{\mathrm{d}y}{\mathrm{d}\tau} = -\frac{\partial U(y)}{\partial y} \tag{11}$$

where $y = |u|^2$ is the dimensionless mode energy. Therefore, taking the steady state mode energy (Eq. (7)) and integrating both sides gives

$$U(y) = \eta y^2 - 4\eta^3 |\tilde{s}_p|^2 \arctan\left(\frac{y-1}{\eta}\right) + K \tag{12}$$

where $K$ is an integration constant. In the bistable regime, Eq. (12) admits two minima and one local maximum. Writing these extrema $y_1, y_2$ and $y_3$ with $y_1 < y_2 < y_3$, potential barriers are defined as

$$\Delta U_{21}(\tau) = U(y_2) - U(y_1), \tag{13a}$$

$$\Delta U_{23}(\tau) = U(y_2) - U(y_3). \tag{13b}$$

These are function of $\tau$ because $|\tilde{s}_p|^2$ is a function of time (see Eq. (4)) in Eq. (12). As a result, the potential barriers are modulated, when $\Delta U_{21}$ is maximum, $\Delta U_{23}$ is minimum, and vice versa.

### C. Derivation of $\delta$ and $\zeta_0$

So that Eq. (10a) and (10b) remain satisfied during the whole modulation period given by Eq. (4), $\zeta_0$ and $\delta$ depends on $\zeta_1$ and $\zeta_2$ and are coupled. Eq. (10a), (10b) and (4) imply that

$$\zeta_1 < \zeta_0 \left(1 + \delta^2 + 2\delta\cos(\tilde{\Omega}\tau)\right) < \zeta_2. \tag{14}$$

The time-averaged dimensionless pump power $|\tilde{s}_p|^2$ is equal to $\frac{\zeta_1+\zeta_2}{2}$ if

$$\zeta_0 \left(1 + \delta^2\right) = \frac{\zeta_1 + \zeta_2}{2}. \tag{15}$$

This relation leads to Eq. (5b). The second condition (Eq. (5a)) can be obtained by subtracting the extrema of $|\tilde{s}_p|^2$ and comparing the result to the difference between $\zeta_2$ and $\zeta_1$ by imposing

$$\zeta_2 - \zeta_1 > 4\delta\zeta_0. \tag{16}$$

By using Eq. (5b) and saturating the inequality, one obtains

$$\delta^2 \frac{\zeta_2 - \zeta_1}{2(\zeta_2 + \zeta_1)} - \delta + \frac{\zeta_2 - \zeta_1}{2(\zeta_2 + \zeta_1)} = 0. \tag{17}$$

This second order equation has two solutions

$$\delta_{\pm} = \frac{\zeta_2 + \zeta_1}{\zeta_2 - \zeta_1} \pm \sqrt{\left(\frac{\zeta_2 + \zeta_1}{\zeta_2 - \zeta_1}\right)^2 - 1} \tag{18}$$

but only $\delta_-$ corresponds to $\delta < 1$, i.e. a signal amplitude smaller than the pump amplitude. The $\kappa < 1$ factor in Eq. (5a) ensures that Eq. (16) is respected with $\delta = \kappa\delta_-$.

### D. Coherent and thermal contributions

As noted, Eq. (1a) belongs to the category of stochastic differential equations (SDE). Therefore, to obtain relevant information about the system, thermodynamic ensemble averages denoted by $\langle . \rangle$ have to be taken. However, as we are dealing with signals, we are interested in their amplitudes, represented by their norm. In such a situation, the reader must be aware that $|\langle . \rangle|^2$ and $\langle |.| \rangle^2$ are different quantities. As an illustration, let us consider the outgoing power $|s_-(t)|^2$.

The coherent part of the output power is obtained by taking first the ensemble average, and then the amplitude [44],

$$s_- \xrightarrow[\text{average}]{\langle . \rangle} \langle s_- \rangle \xrightarrow[\text{amplitude squared}]{|.|^2} |\langle s_- \rangle|^2 = \text{coherent output.}$$

By taking the ensemble average first, the stochastic contributions are cancelled out, as noise sources are centered Gaussian random variables.

The total output power is therefore obtained by computing

$$s_- \xrightarrow[\text{amplitude squared}]{|.|^2} |s_-|^2 \xrightarrow[\text{average}]{\langle . \rangle} \langle |s_-|^2 \rangle = \text{total output.}$$

The difference $\langle |s_-|^2 \rangle - |\langle s_- \rangle|^2$, or the variance of $s_-$, is the thermal contribution [44] to the output power as it derives from thermal noise.

To obtain the spectra, one must pay attention to the order of operations when taking the Fourier transform. Indeed, $\langle |s_-(\omega)|^2 \rangle \neq \langle |s_-|^2 \rangle(\omega)$. In this work, we always consider $|s_-(\omega)|^2$. On the one hand, to obtain the coherent spectral density, the Fourier transform of the time series $s_-(t)$ is taken first. Then, the ensemble average of all Fourier transforms is computed. Finally, taking the absolute value squared leads to the coherent contribution. On the other hand, to get the total spectral density, the absolute value squared of all Fourier transforms is collected, before ensemble-averaging them. Finally, thermal radiation can be computed from subtracting $\langle |s_-(\omega)|^2 \rangle$ and $|\langle s_-(\omega) \rangle|^2$ as in the time domain.

**Funding.** This work was supported by the Fonds pour la Formation à la Recherche dans l'Industrie et dans l'Agriculture (FRIA) and by the Fonds National de Recherche Scientifique (FNRS) in Belgium.

**Acknowledgments.** Computational resources have been provided by the Consortium des Équipements de Calcul Intensif (CÉCI), funded by the FNRS under Grant No. 2.5020.11 and by the Walloon Region. We thank Alejandro Rodriguez for useful discussions.

**Disclosures.** The authors declare no conflicts of interest.

**Data availability.** Data underlying the results presented in this paper are not publicly available at this time but may be obtained from the authors upon reasonable request.

## References

1. Z. Yu and S. Fan, "Complete optical isolation created by indirect interband photonic transitions," Nat. Photon. **3**, 91–94 (2009).
2. H. Lira, Z. Yu, S. Fan, and M. Lipson, "Electrically Driven Nonreciprocity Induced by Interband Photonic Transition on a Silicon Chip," Phys. Rev. Lett. **109**, 033901 (2012).

3. Y. Hadad, D. L. Sounas, and A. Alu, “Space-time gradient metasurfaces,” Phys. Rev. B **92**, 100304 (2015).
4. D. L. Sounas and A. Alù, “Non-reciprocal photonics based on time modulation,” Nat. Photon. **11**, 774–783 (2017).
5. G. Altares Menendez and B. Maes, “Selective frequency conversion with coupled time-modulated cavities,” Phys. Rev. B **100**, 014306 (2019).
6. S. Buddhiraju, W. Li, and S. Fan, “Photonic Refrigeration from Time-Modulated Thermal Emission,” Phys. Rev. Lett. **124**, 077402 (2020).
7. M. Dykman, ed., *Fluctuating Nonlinear Oscillators: From Nanomechanics to Quantum Superconducting Circuits* (Oxford University Press, 2012).
8. T. J. Kippenberg and K. J. Vahala, “Cavity Opto-Mechanics,” Opt. Express **15**, 17172–17205 (2007).
9. L.-A. Wu, M. Xiao, and H. J. Kimble, “Squeezed states of light from an optical parametric oscillator,” J. Opt. Soc. Am. B **4**, 1465–1476 (1987).
10. L. Gammaitoni, P. Hänggi, P. Jung, and F. Marchesoni, “Stochastic resonance,” Rev. Mod. Phys. **70**, 223–287 (1998).
11. B. McNamara and K. Wiesenfeld, “Theory of stochastic resonance,” Phys. Rev. A **39**, 4854–4869 (1989).
12. T. Wellens, V. Shatokhin, and A. Buchleitner, “Stochastic resonance,” Rep. Prog. Phys. **67**, 45–105 (2003).
13. H. A. Kramers, “Brownian motion in a field of force and the diffusion model of chemical reactions,” Physica **7**, 284–304 (1940).
14. B. McNamara, K. Wiesenfeld, and R. Roy, “Observation of Stochastic Resonance in a Ring Laser,” Phys. Rev. Lett. **60**, 2626–2629 (1988).
15. H. Gang, T. Ditzinger, C. Z. Ning, and H. Haken, “Stochastic resonance without external periodic force,” Phys. Rev. Lett. **71**, 807–810 (1993).
16. R. Bartussek, P. Hänggi, and P. Jung, “Stochastic resonance in optical bistable systems,” Phys. Rev. E **49**, 3930–3939 (1994).
17. F. Marino, M. Giudici, S. Barland, and S. Balle, “Experimental Evidence of Stochastic Resonance in an Excitable Optical System,” Phys. Rev. Lett. **88**, 040601 (2002).
18. I. Y. Lee, X. Liu, B. Kosko, and C. Zhou, “Nanosignal Processing: Stochastic Resonance in Carbon Nanotubes That Detect Subthreshold Signals,” Nano Lett. **3**, 1683–1686 (2003).
19. D. V. Dylov and J. W. Fleischer, “Nonlinear self-filtering of noisy images via dynamical stochastic resonance,” Nat. Photon. **4**, 323–328 (2010).
20. H. Abbaspour, S. Trebaol, F. Morier-Genoud, M. T. Portella-Oberli, and B. Deveaud, “Stochastic Resonance in Collective Exciton-Polariton Excitations inside a GaAs Microcavity,” Phys. Rev. Lett. **113**, 057401 (2014).
21. H. Abbaspour, S. Trebaol, F. Morier-Genoud, M. T. Portella-Oberli, and B. Deveaud, “Spinor stochastic resonance,” Phys. Rev. B **91**, 155307 (2015).
22. F. Monifi, J. Zhang, Ş. K. Özdemir, B. Peng, Y.-x. Liu, F. Bo, F. Nori, and L. Yang, “Optomechanically induced stochastic resonance and chaos transfer between optical fields,” Nat. Photon. **10**, 399–405 (2016).
23. F. Ricci, R. A. Rica, M. Spasenović, J. Gieseler, L. Rondin, L. Novotny, and R. Quidant, “Optically levitated nanoparticle as a model system for stochastic bistable dynamics,” Nat. Commun. **8**, 15141 (2017).
24. A. Chowdhury, S. Barbay, M. G. Clerc, I. Robert-Philip, and R. Braive, “Phase Stochastic Resonance in a Forced Nanoelectromechanical Membrane,” Phys. Rev. Lett. **119**, 234101 (2017).
25. T. Wagner, P. Talkner, J. C. Bayer, E. P. Rugeramigabo, P. Hänggi, and R. J. Haug, “Quantum stochastic resonance in an a.c.-driven single-electron quantum dot,” Nat. Phys. **15**, 330–334 (2019).
26. A. Krawiecki and J. A. Hołyst, “Stochastic resonance as a model for financial market crashes and bubbles,” Phys. A: Stat. Mech. Appl. **317**, 597–608 (2003).
27. J.-C. Li, C. Li, and D.-C. Mei, “Effects of time delay on stochastic resonance of the stock prices in financial system,” Phys. Lett. A **378**, 1997–2000 (2014).
28. R.-W. Zhou, G.-Y. Zhong, J.-C. Li, Y.-X. Li, and F. He, “Stochastic resonance of periodic volatility in financial markets with stock crashes,” Mod. Phys. Lett. B **32**, 1850290 (2018).
29. D. S. Leonard and L. E. Reichl, “Stochastic resonance in a chemical reaction,” Phys. Rev. E **49**, 1734–1737 (1994).
30. A. Guderian, G. Dechert, K.-P. Zeyer, and F. W. Schneider, “Stochastic Resonance in Chemistry. 1. The Belousov-Zhabotinsky Reaction,” J. Phys. Chem. **100**, 4437–4441 (1996).
31. A. Förster, M. Merget, and F. W. Schneider, “Stochastic Resonance in Chemistry. 2. The Peroxidase-Oxidase Reaction,” J. Phys. Chem. **100**, 4442–4447 (1996).
32. W. Hohmann, J. Müller, and F. W. Schneider, “Stochastic Resonance in Chemistry. 3. The Minimal-Bromate Reaction,” J. Phys. Chem. **100**, 5388–5392 (1996).
33. J. K. Douglass, L. Wilkens, E. Pantazelou, and F. Moss, “Noise enhancement of information transfer in crayfish mechanoreceptors by stochastic resonance,” Nature **365**, 337–340 (1993).
34. S. M. Bezrukov and I. Vodyanoy, “Noise-induced enhancement of signal transduction across voltage-dependent ion channels,” Nature **378**, 362–364 (1995).
35. F. Jaramillo and K. Wiesenfeld, “Mechanoelectrical transduction assisted by Brownian motion: A role for noise in the auditory system,” Nat. Neurosci. **1**, 384–388 (1998).
36. D. F. Russell, L. A. Wilkens, and F. Moss, “Use of behavioural stochastic resonance by paddle fish for feeding,” Nature **402**, 291–294 (1999).
37. D. Petracchi, I. C. Gebeshuber, L. J. DeFelice, and A. V. Holden, “Stochastic resonance in biological systems,” Chaos Solitons Fractals **11**, 1819–1822 (2000).

38. T. Mori and S. Kai, "Noise-Induced Entrainment and Stochastic Resonance in Human Brain Waves," Phys. Rev. Lett. **88**, 218101 (2002).
39. P. Hänggi, "Stochastic Resonance in Biology How Noise Can Enhance Detection of Weak Signals and Help Improve Biological Information Processing," ChemPhysChem **3**, 285–290 (2002).
40. R. Benzi, "Stochastic resonance: From climate to biology," Nonlinear Process. Geophys. **17**, 431–441 (2010).
41. R. Wallace, D. Wallace, and H. Andrews, "AIDS, Tuberculosis, Violent Crime, and Low Birthweight in Eight US Metropolitan Areas: Public Policy, Stochastic Resonance, and the Regional Diffusion of Inner-City Markers," Environ. Plan. A **29**, 525–555 (1997).
42. R. Wallace and D. Wallace, "Resilience and Persistence of the Synergism of Plagues: Stochastic Resonance and the Ecology of Disease, Disorder and Disinvestment in US Urban Neighborhoods," Environ. Plan. A **29**, 789–804 (1997).
43. K. J. H. Peters, Z. Geng, K. Malmir, J. M. Smith, and S. R. K. Rodriguez, "Extremely Broadband Stochastic Resonance of Light and Enhanced Energy Harvesting Enabled by Memory Effects in the Nonlinear Response," Phys. Rev. Lett. **126**, 213901 (2021).
44. C. Khandekar, Z. Lin, and A. W. Rodriguez, "Thermal radiation from optically driven Kerr ($\chi^{(3)}$) photonic cavities," Appl. Phys. Lett. **106**, 151109 (2015).
45. M. I. Dykman, D. G. Luchinsky, R. Mannella, P. V. E. McClintock, N. D. Stein, and N. G. Stocks, "Supernarrow spectral peaks and high-frequency stochastic resonance in systems with coexisting periodic attractors," Phys. Rev. E **49**, 1198–1215 (1994).
46. V. Lousse and J. P. Vigneron, "Use of Fano resonances for bistable optical transfer through photonic crystal films," Phys. Rev. B **69**, 155106 (2004).
47. B. Maes, P. Bienstman, and R. Baets, "Switching in coupled nonlinear photonic-crystal resonators," J. Opt. Soc. Am. B **22**, 1778–1784 (2005).
48. B. Maes, M. Soljačić, J. D. Joannopoulos, P. Bienstman, R. Baets, S.-P. Gorza, and M. Haelterman, "Switching through symmetry breaking in coupled nonlinear micro-cavities," Opt. Express **14**, 10678–10683 (2006).
49. B. Maes, P. Bienstman, and R. Baets, "Symmetry breaking with coupled Fano resonances," Opt. Express **16**, 3069–3076 (2008).
50. B. Maes, M. Fiers, and P. Bienstman, "Self-pulsing and chaos in short chains of coupled nonlinear microcavities," Phys. Rev. A **80**, 033805 (2009).
51. M. Marconi, F. Raineri, A. Levenson, A. M. Yacomotti, J. Javaloyes, S. H. Pan, A. E. Amili, and Y. Fainman, "Mesoscopic limit cycles in coupled nanolasers," Phys. Rev. Lett. **124**, 213602 (2020).
52. C. Khandekar, A. Pick, S. G. Johnson, and A. W. Rodriguez, "Radiative heat transfer in nonlinear Kerr media," Phys. Rev. B **91**, 115406 (2015).
53. P. E. Kloeden and E. Platen, *Numerical Solution of Stochastic Differential Equations*, no. 23 in Applications of Mathematics (Springer, 1992).
54. K. Jacobs, *Stochastic Processes for Physicists: Understanding Noisy Systems* (Cambridge University Press, 2010).
55. R. L. Stratonovich, "Some Markov methods in the theory of stochastic processes in nonlinear dynamical systems," in *Noise in Nonlinear Dynamical Systems: Volume 1: Theory of Continuous Fokker-Planck Systems,* vol. 1 F. Moss and P. V. E. McClintock, eds. (Cambridge University Press, 1989), pp. 16–71.
56. N. G. van Kampen, *Stochastic Processes in Physics and Chemistry* (North Holland, 2007), 3rd ed.
57. C. Nardini, S. Gupta, S. Ruffo, T. Dauxois, and F. Bouchet, "Kinetic theory of nonequilibrium stochastic long-range systems: Phase transition and bistability," J. Stat. Mech. **2012**, P12010 (2012).
58. M. I. Dykman, R. Mannella, P. V. E. McClintock, and N. G. Stocks, "Fluctuation-induced transitions between periodic attractors: Observation of supernarrow spectral peaks near a kinetic phase transition," Phys. Rev. Lett. **65**, 48–51 (1990).
59. C. Stambaugh and H. B. Chan, "Supernarrow Spectral Peaks near a Kinetic Phase Transition in a Driven Nonlinear Micromechanical Oscillator," Phys. Rev. Lett. **97**, 110602 (2006).
60. L. Caspani, R. P. M. Kaipurath, M. Clerici, M. Ferrera, T. Roger, J. Kim, N. Kinsey, M. Pietrzyk, A. Di Falco, V. M. Shalaev, A. Boltasseva, and D. Faccio, "Enhanced Nonlinear Refractive Index in $\varepsilon$-Near-Zero Materials," Phys. Rev. Lett. **116**, 233901 (2016).
61. P. Guo, R. D. Schaller, L. E. Ocola, B. T. Diroll, J. B. Ketterson, and R. P. H. Chang, "Large optical nonlinearity of ITO nanorods for sub-picosecond all-optical modulation of the full-visible spectrum," Nat Commun **7**, 12892 (2016).
62. K. Pang, M. Z. Alam, Y. Zhou, C. Liu, O. Reshef, K. Manukyan, M. Voegtle, A. Pennathur, C. Tseng, X. Su, H. Song, Z. Zhao, R. Zhang, H. Song, N. Hu, A. Almaiman, J. M. Dawlaty, R. W. Boyd, M. Tur, and A. E. Willner, "Adiabatic Frequency Conversion Using a Time-Varying Epsilon-Near-Zero Metasurface," Nano Lett. **21**, 5907–5913 (2021).
63. E. Galiffi, R. Tirole, S. Yin, H. Li, S. Vezzoli, P. A. Huidobro, M. G. Silveirinha, R. Sapienza, A. Alù, and J. B. Pendry, "Photonics of time-varying media," AP **4**, 014002 (2022).
64. M. Z. Alam, I. De Leon, and R. W. Boyd, "Large optical nonlinearity of indium tin oxide in its epsilon-near-zero region," Science **352**, 795–797 (2016).
65. M. Soljačić, M. Ibanescu, S. G. Johnson, Y. Fink, and J. D. Joannopoulos, "Optimal bistable switching in nonlinear photonic crystals," Phys. Rev. E **66**, 055601 (2002).
66. S. H. Strogatz, *Nonlinear Dynamics And Chaos* (Westview Press, 1994).